



A New Trajectory Tracking Framework for Autonomous Vehicles with In-wheel Motors

Hamid Rahmani^{1*}, Abbas Aliabadi², Ali Ghaffari³, Shahram Azadi⁴

¹Ph.D Candidate, Mechanical Engineering, K.N.Toosi University of Technology, Tehran, Iran.

²CEO, MAPNA Group, Tehran, Iran.

³Professor, Mechanical Engineering, K.N.Toosi University of Technology, Tehran, Iran.

⁴Associate Professor, Mechanical Engineering, K.N.Toosi University of Technology, Tehran, Iran.

ARTICLE INFO

Article history:

Received: 19 Apr

Accepted: 7 Jun

Published: 27 Jun

Keywords:

Active Front Steering

Autonomous Vehicles

In-wheel Electric Motors

Sliding Mode Control

Torque Distribution

Trajectory Tracking

ABSTRACT

The coordinated control of autonomous electric vehicles with in-wheel motors is classified as over-actuated control problems requiring a precise control allocation strategy. This paper addresses the trajectory tracking problem of autonomous electric vehicles equipped with four independent in-wheel motors and active front steering. Unlike other available methods presenting optimization formulation to handle the redundancy, in this paper, the constraints have been applied directly using the kinematic relations of each wheel. Four separate sliding mode controllers are designed in such a way that they ensure the convergence of tracking errors. The lateral controller is also designed to determine the front steering angles to eliminate lateral tracking errors. To appraise the performance of the proposed control strategy, a co-simulation is carried out in MATLAB/Simulink and Carsim software. The results show that the proposed control strategy has enabled the vehicle to follow the reference path. The tracking errors of longitudinal and lateral positions and the velocity are limited to [-2.6, 4] cm, [-4.5, 3.3] cm, and [-0.2, 0.4] m/s, respectively and the error signals for the heading angle and yaw rate lie in the bounds of $\pm 0.3^\circ$ and $\pm 2.7^\circ/\text{s}$, respectively. Furthermore, the proposed control system shows promising results in the presence of uncertainties including the mass and moment of inertia, friction coefficient, and the wind disturbances.

1. Introduction

The market share and ongoing plans of the world's major automotive industries prefigure that the future generation of transportation is autonomous internal combustion and autonomous electric vehicles (AEVs) [1]. In recent years, numerous environmental crises and issues related to the energy economy have attracted the attention of governments and automotive industries on electrification that have increased the demand for electric vehicles [2, 3].

In addition, extensive research has been conducted and is ongoing to design various structures related to the electrical actuators, like: steering, braking, and propulsion systems.

Electric vehicles with in-wheel motors (IWMs) have the advantage of applying the torque of each wheel, separately. In contrast, the force and torque allocation in the front and rear axles of conventional vehicles are executed mechanically with predefined ratios [4]. Accordingly, the number of inputs exceeds the number of desired

*Corresponding Author

Email Address: hrahmani@mail.kntu.ac.ir
<http://doi.org/10.22068/ase.2023.638>

outputs. Thereby, an over-actuator problem arises that requires an intricate control system to distribute the torque acting on each wheel. Generally speaking, there are two approaches in the literature to deal with this problem, including the direct and indirect actuators assignment.

The direct actuator assignment strategy has the advantage of real-time calculations, and the limitations of actuators can be imposed directly [5, 6]. Notwithstanding, simplifications such as linearization of the tire model [7], or the vehicle dynamics model simplifications may be required during controller design [8, 9]. The purpose of this kind of controller is either to regulate the vehicle states [8] or to track a desired trajectory [9]. Nevertheless, some studies assume a constant longitudinal speed and focus on the design of four-wheel independent steering angle controllers [10, 11]. Another advantage of this approach is that more numbers of tracking errors can be managed independently [12-14], as opposed to conventional vehicles, which have fewer input variables than outputs and suffer from limited authority for controlling the tracking errors.

On the other hand, the indirect actuator assignment approach focuses on the force distribution among the wheels. Therefore, the control inputs in this approach are the longitudinal and lateral forces of each wheel. The superiority of this approach lies in the explicit handling of the tire forces in the control system design, which is greatly beneficial in predicting and precluding undesirable situations, like understeer and oversteer [15]. Most of the proposed strategies with this approach utilize a hierarchical structure to first track the desired motion of the vehicle's center of gravity (CG), which results in the total force and yaw moment at and around the vehicle's CG [16-18]. The distribution of these variables among the wheels requires a sophisticated optimization scheme. The corresponding cost functions for the optimization proposed in the literature include the squared terms of tire forces in the form of inequality and equality constraints [19, 20], the sum of longitudinal force utilization of each tire [21], the sum of each tire's dissipated energy [22], equal friction usage constraints [17, 18], and the weighted sum of the variance and mean

value of the friction usage of each tire [23-25]. One of the drawbacks of these methods is the high computational burdens initiated by solving the optimization problem. Other disadvantages of this approach include the non-convexity of constraints and the local minimum. The mentioned drawbacks listed for the two previously discussed approaches highlight the need for more efficient methods [26], which is the main motivation of the present work.

This paper focuses on the design of a robust integrated control strategy to determine the front steering angle and the torque of each wheel in the task of trajectory tracking. The contributions of this research are listed as bellow:

- 1) Unlike other available methods presenting optimization formulation to handle the redundancy, in this paper, the constraints have been applied directly using kinematic relations on each wheel. The limitations related to the vehicle dynamics and the stability of its motion are considered during the design of the reference path, curvature, speed, and acceleration profiles for the vehicle's CG on the lane-change maneuver. All of these constraints are mapped into the wheel's coordinates using the kinematic relations. The proposed method enables the AEV to calculate the error signals of each wheel without intricate time-consuming iterative calculations.
- 2) To calculate the steering angle of the front wheels, a robust sliding mode control (SMC) is designed, which is able to converge the tracking errors of lateral motion and the heading angle of the AEV. The steering angle is closely associated with the direction of the velocity vector of the front wheels and its desired speed direction, related to the design of the corresponding longitudinal controller.
- 3) The proof of stability for both longitudinal and lateral controllers, while the AEV is following the lane-change reference path, is provided by introducing some separate Lyapunov functions.

The rest of the paper is organized as follows. Section 2 describes how the kinematic equations of each wheel are extracted. Also, the dynamic models used in the design of the longitudinal and lateral controller are illustrated, briefly. Then, the lane-change reference path to be followed is presented. Next, the control methodology, including the steering controller and the distributed longitudinal controller of each wheel, is demonstrated in Section 3. Then, the results of the proposed control scheme are provided and discussed in Section 4. Also, the comparison of the results and the effects of uncertainties are presented. The concluding remarks and the future path of this research are highlighted in section 5.

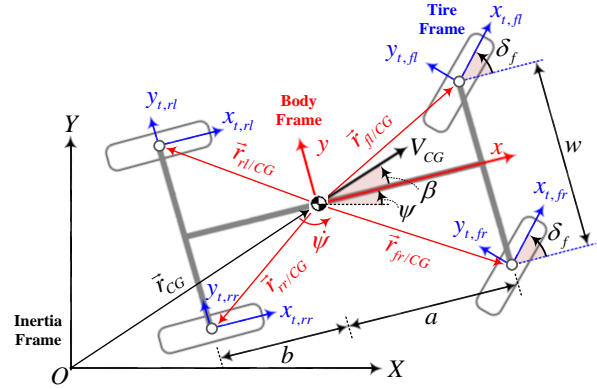


Figure 1: Position and orientation for the CG of the AEV and the reference path.

2. Problem Formulation and Modeling

In this section, the kinematic model of the AEV including the position, velocity, and acceleration of each wheel, is described. Also, the lateral two degrees of freedom (DOF) bicycle model is introduced for the steering control design. Furthermore, the reference path and the admissible velocity and acceleration profiles on the reference path are highlighted.

2.1. Kinematic Model

Figure 1 shows the 4-wheel kinematic model of the AEV. The inertia and body frames are shown by (X, Y) and (x, y) , respectively, and $(x_{t,i}, y_{t,i})$, $i \in \{fl, fr, rl, rr\}$ denotes the tire frame of the front left, front right, rear left, and rear right wheel. The angle between the longitudinal direction of the vehicle and the direction $x_{t,i}$ of the front wheels is the steering angle δ_f , and the slip angle between the velocity vector V_{CG} and the longitudinal x -direction is represented by β . The heading and yaw rate of the AEV are indicated by ψ and $\dot{\psi}$, respectively.

The vector $\vec{r}_{i/CG}$ in Figure 1 express the position of the center of each wheel relative to the CG. The track width and the distance from CG to the front and rear axles are denoted by w , a and b . The relative motion concept is used to find the position of each wheel, as in (1).

$$\vec{R}_i = \vec{r}_{CG} + \mathbf{R}_\psi \vec{r}_{i/CG}, \quad i \in \{fl, fr, rl, rr\} \quad (1)$$

Where \vec{R}_i and \vec{r}_{CG} represent the position vector of the vehicle's CG and the center of each wheel expressed in inertial coordinates, respectively. The vectors $\vec{r}_{i/CG}$ denote the position of the center of each wheel expressed in the body coordinate, according to Figure 1, are given as

$$\begin{aligned} \vec{r}_{fl/CG} &= \begin{bmatrix} a \\ w/2 \end{bmatrix}, & \vec{r}_{fr/CG} &= \begin{bmatrix} a \\ -w/2 \end{bmatrix}, \\ \vec{r}_{rl/CG} &= \begin{bmatrix} -b \\ w/2 \end{bmatrix}, & \vec{r}_{rr/CG} &= \begin{bmatrix} -b \\ -w/2 \end{bmatrix}, \end{aligned} \quad (2)$$

The rotation matrix \mathbf{R}_ψ in (1) is obtained from the following equation.

$$\begin{bmatrix} X \\ Y \end{bmatrix} = \mathbf{R}_\psi \begin{bmatrix} x \\ y \end{bmatrix} \Rightarrow \mathbf{R}_\psi = \begin{bmatrix} \cos \psi & -\sin \psi \\ \sin \psi & \cos \psi \end{bmatrix} \quad (3)$$

The velocity vector of each wheel is calculated by taking the time derivative of (1), as bellow

$$\vec{V}_i = \vec{v}_{CG} + \mathbf{R}_\psi (\dot{\psi} \times \vec{r}_{i/CG} + \vec{v}_{i,rel}) \quad (4)$$

Where \vec{V}_i and \vec{v}_{CG} represent the velocity vector of the vehicle's CG and the center of each wheel expressed in inertial coordinates, respectively. The vector $\vec{v}_{i,rel}$ denotes the relative velocity of the center of each wheel with respect to the body coordinate, which is equal to zero, since the

relative distance from CG to the center of each wheel has a constant value.

The acceleration vector of each wheel is determined by taking twice the time derivative of (1), which results in

$$\begin{aligned} \vec{A}_i &= \vec{a}_{CG} + \mathbf{R}_\psi [\dot{\vec{\psi}} \times (\dot{\vec{\psi}} \times \vec{r}_{i/CG}) \dots \\ &\dots + \ddot{\vec{\psi}} \times \vec{r}_{i/CG} + 2\dot{\vec{\psi}} \times \vec{v}_{i,rel} + \vec{a}_{i,rel}] \end{aligned} \quad (5)$$

Where \vec{A}_i and \vec{a}_{CG} represent the acceleration vector of the vehicle's CG and the center of each wheel expressed in inertial coordinates, respectively. For the same reason that $\vec{v}_{i,rel} = \vec{0}$, the acceleration $\vec{a}_{i,rel}$ also becomes zero.

It is important to note that the position, velocity, and acceleration vectors in (1), (4), and (5), are expressed in the inertial frame. However, in the process of designing the sliding surface based on the tracking error of each wheel, the error signal includes the difference between the actual traveled path and the desired traveled path in the coordinates of each tire. Therefore, the vectors \vec{R}_i , \vec{V}_i , and \vec{A}_i must be rotated enough to be expressed in the coordinates of each tire, without changing the amplitude. To fulfill this purpose, the following transformations are introduced.

$$\vec{\zeta}_i^t = \mathbf{R}_{-(\delta_i+\psi)} \vec{\zeta}_i, \quad \zeta \in \{R, V, A\} \quad (6)$$

Where \vec{R}_i^t , \vec{V}_i^t , and \vec{A}_i^t represent the position, velocity, and acceleration vectors on each tire's coordinate. In addition, the steering angle $\delta_i = 0$ for $i \in \{rl, rr\}$ and $\delta_i = \delta_f$ for the front left and front right wheels in (6).

2.2. Control-oriented Dynamic Models

The free body diagrams for the lateral dynamic model of the vehicle planar motion, along with the rotational dynamic of each wheel are presented in Figure 2. The bicycle model in Figure 2-a, offers a simple representation of the vehicle's rotational and lateral dynamics. However, it is not able to capture the dynamic load transfer (DLT), nor the roll, pitch, and vertical dynamics of the suspension system of

the vehicle. The longitudinal and lateral forces of the central front and rear wheels are shown as $f_{xt,i}$ and $f_{yt,i}$, where $f_{xt,f} = f_{xt,fl} + f_{xt,fr}$, $f_{xt,r} = f_{xt,rl} + f_{xt,rr}$, $f_{yt,r} = f_{yt,fl} + f_{yt,fr}$, and $f_{yt,r} = f_{yt,rl} + f_{yt,rr}$. The rotational speed of each wheel is indicated by ω_i and the driving and braking torque of each wheel are denoted by $T_{a,i}$ and $T_{b,i}$, respectively.

Now, assuming the vehicle as a rigid body and applying the force and moment balance at and around the CG, the lateral equations of the motion can be extracted.

$$\begin{aligned} a: \quad ma_y &= [f_{yt,r} + f_{yt,f} \cos \delta_f \dots \\ &\dots + f_{xt,f} \sin \delta_f] \\ b: \quad I_{zz}\ddot{\psi} &= [-bf_{yt,r} + a(f_{yt,f} \cos \delta_f \dots \\ &\dots + f_{xt,f} \sin \delta_f)] \end{aligned} \quad (7)$$

Where the lateral acceleration is denoted by $a_y = \ddot{y} + \dot{x}\dot{\psi}$ [21]. The relationship between the longitudinal and lateral combined slips and the DLT model, in order to produce the longitudinal and lateral forces applied on each tire, is adapted from [27]. This nonlinear combined slip Pacejka tire model provides an estimate for the lateral force as a function of lateral slip α_i , longitudinal slip $s_{x,i}$, friction μ , and the normal force $F_{z,i}$ acting on each tire.

Similarly, the rotational dynamics of each wheel are obtained by applying the torque balance around the lateral axis $y_{t,i}$ in Figure 2-b, which results in

$$I_{yt,i}\dot{\omega}_i = -R_i f_{xt,i} + \begin{cases} T_{a,i} & \text{Driving} \\ T_{b,i} & \text{Braking} \end{cases} \quad (8)$$

Where R_i and $I_{yt,i}$ represent the effective radius and mass moment of inertia of each wheel. Equations (7) and (8) will be utilized later for the design of lateral and longitudinal controllers, respectively.

2.3. Reference Trajectory

Figure 3 illustrates the desired path, including a lane change maneuver from the current lane.

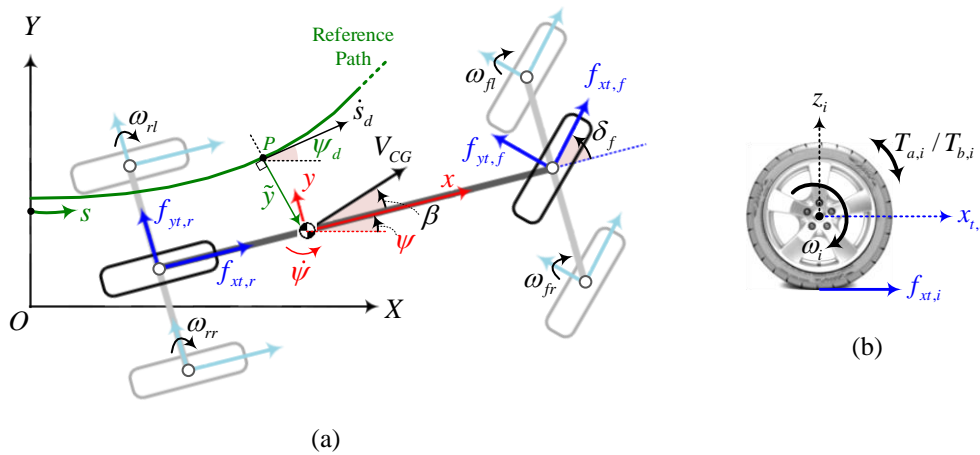


Figure 2: Free body diagrams, (a) Lateral motion of the AEV, (b) Rotating motion of each wheel.

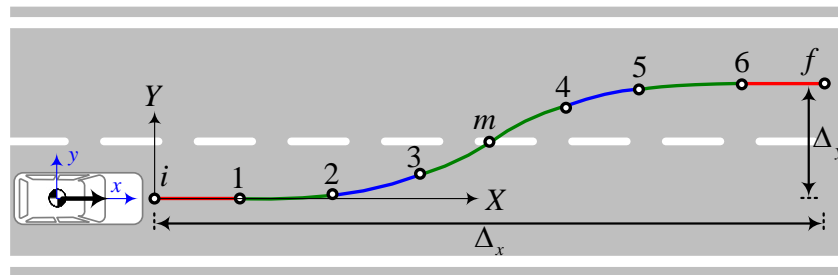


Figure 3: The reference lane-change path, with $[\Delta_x, \Delta_y]=[70, 3.7]$ m.

According to Figure 3, the lane-change path starts with a straight line (i-1) and ends with another straight line (6-f), and the middle part of the lane-change consists of two consecutive elementary paths (1-2-3-m and m-4-5-6). Each elementary path consists of two clothoid and one arc of a circle, each of which has curvatures $\kappa(s) = \sigma s$ and $\kappa = 1/R$, respectively, where R is the radius of the circle and σ is the rate of change of the curvature in the clothoid. To acquire the reference longitudinal and lateral positions and the reference yaw angle, one can integrate the following equations, numerically.

$$\begin{bmatrix} \psi_a(s) \\ X_a(s) \\ Y_a(s) \end{bmatrix} = \int_0^s \begin{bmatrix} \kappa(\xi) \\ \cos \psi(\xi) \\ \sin \psi(\xi) \end{bmatrix} d\xi \quad (9)$$

Where $s \in [0, L_p]$ indicates the path parameter and L_p is the length of each elementary path. The remaining steps to design the reference path for the lane-change maneuver which leads to generating a continuous and smooth path and at

the same time involves real-time calculations, are adapted from [28].

Up to this point, a reference lane-change path is generated with specified longitudinal and lateral positions and the heading angle along the path. To determine the quality of navigation, it is needed to design the speed and acceleration profiles while traveling the reference path. The reference path cannot be traveled by any arbitrary velocity and acceleration profiles. One of the limitations of the design is the curvature of the path that the vehicle travels. Another constraint is the amount of friction that exists between the road surface and the contact patch of the tires. Here we assume a point mass model for the vehicle, which provides an approximate value $a_Y(s) = V_X^2(s)\kappa(s)$ for the lateral acceleration. Then, the admissible accelerations are given in the form of the following constraint.

$$[a_X^2(s) + a_Y^2(s)]^{1/2} \leq a_0 = \mu g \quad (10)$$

Where μ shows the average friction coefficient

and g denotes the gravitational acceleration. Therefore, the longitudinal acceleration on the path is given by the following equation.

$$a_x(s) = \min\{[a_0^2 - (V_x^2(s)\kappa(s))^2]^{1/2}, a_{x,max}\} \quad (11)$$

Where $a_{x,max}$ denotes the maximum allowable longitudinal acceleration provided by the AEV. This allowable acceleration is set to be in the comfort zone of the passenger, as described in [29]. Thereafter, with the assumption of constant acceleration between each of the two points in Figure 3 and integrating (11) along the path length s , the speed profile is obtained. In Figure 3, the speed of the arc segments (2-3 and 4-5) have a constant value $V_{arc} = [a_0/\kappa_{arc}]^{1/2}$, depending on the curvature. Subsequently, two possible speed profiles are made corresponding to two constant curvatures in the lane-change path. The actual speed profile must be selected sufficiently small so that during the lane-change path, it has a lower value than both of the mentioned speed profiles.

Figure 4 depicts the desired actual speed profile and the two possible speed profiles $V_{23}(s)$ and $V_{45}(s)$ corresponding to the constant curvatures κ_{23} and κ_{45} of the arc segments. It becomes apparent that before the point C in Figure 4, the speed corresponding to the curvature κ_{23} has a lower value and therefore it is selected as the actual speed profile in the interval $s \in [0, L_C]$. However, after the point C on Figure 4, due to the lower speed related to the

curvature κ_{45} , this curve is selected as the actual speed profile, and the corresponding actual longitudinal and lateral accelerations are selected in a similar procedure.

3. Control Methodology

The overall scheme of the proposed controller including the separate control of the torque applied to each wheel and the control of the front steering angle of the AEV is shown in Figure 5. The longitudinal motion of the vehicle is taken into control by four separate SMC each of which attempts to fulfill the constraints related to the kinematic quantities of each wheel described in (1) to (6). These torques are designed in such a way that the position and velocity of the vehicle's CG converge toward their corresponding desired values. Thanks to the real-time calculations of this approach to applying the constraints, the issues related to the computational burden caused by solving an optimization problem vanish. Also, the lateral and heading errors of the vehicle during the motion are made to converge to zero by considering the possible uncertainties, using an SMC controller.

3.1. Longitudinal Control: Driving / Braking Torques

In To begin with, note that the desired kinematic components of each wheel are obtained using equations (1) to (6). The sliding surface of each wheel is defined as combination

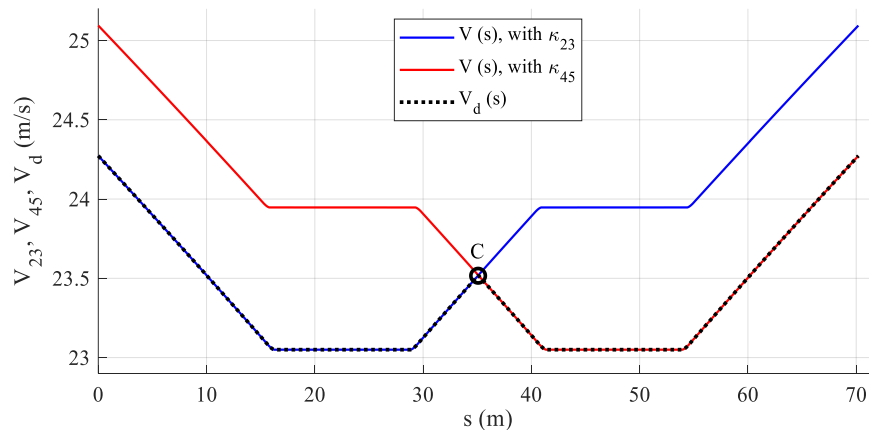


Figure 4: The desired speed profile $V_d(s)$ and the two possible speed profiles V_{23} and V_{45} , on the lane-change path.

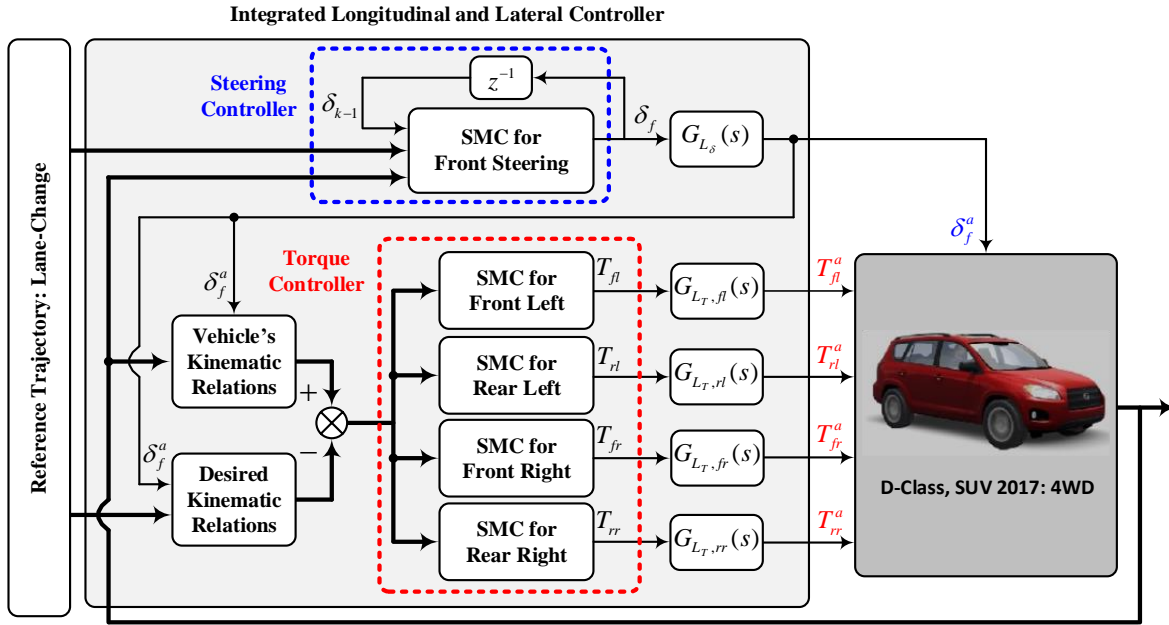


Figure 5: The proposed longitudinal and lateral control strategy for trajectory tracking.

of the longitudinal position and velocity errors, which gives

$$S_{T,i} = \dot{\hat{x}}_i^t + \lambda_{T,i} \hat{x}_i^t = (\dot{x}_i^t - \dot{x}_{d,i}^t) + \lambda_{T,i}(x_i^t - x_{d,i}^t) \quad (12)$$

Where $\lambda_{T,i}$ represents an adjustable control parameter, $x_{d,i}^t$ and $\dot{x}_{d,i}^t$ denote the desired longitudinal position and velocity expressed in each tire's coordinates. Then, with the assumption of ideal estimation on the sliding surface, the time derivative of (12) is set to be zero, which results in the following expression for the longitudinal acceleration.

$$\dot{S}_{T,i} = \ddot{\hat{x}}_i^t + \lambda_{T,i} \dot{\hat{x}}_i^t \Rightarrow \ddot{x}_i^t = \ddot{x}_{d,i}^t - \lambda_{T,i}(\dot{x}_i^t - \dot{x}_{d,i}^t) \quad (13)$$

Now, we must involve the rotational dynamic of each wheel in (8) with the longitudinal acceleration \ddot{x}_i^t in (13). For this purpose, one can utilize the longitudinal slip $s_{xt,i}$ which relates the linear and rotational velocity of each wheel, as bellow.

$$s_{xt,i} = (R_i \omega_i - \dot{x}_i^t) / \max\{\dot{x}_i^t, R_i \omega_i\} \quad (14)$$

Supplementarily, taking the time derivative of (14) yields

$$\dot{s}_{xt,i} = \begin{cases} \frac{R_i(\dot{x}_i^t \dot{\omega}_i - \ddot{x}_i^t \omega_i)}{(\dot{x}_i^t)^2} & \dot{x}_i^t \geq R_i \omega_i \\ \frac{(\dot{x}_i^t \dot{\omega}_i - \ddot{x}_i^t \omega_i)}{R_i \omega_i^2} & \dot{x}_i^t < R_i \omega_i \end{cases} \quad (15)$$

Then, solving (15) for $\dot{\omega}_i$ and replacing into (8), provides the following equation for the torque T_i .

$$T_i = R_i f_{xt,i} \dots + I_{yt,i} \begin{cases} \frac{\dot{s}_{xt,i} \dot{x}_i^t}{R_i} + \frac{\omega_i \ddot{x}_i^t}{\dot{x}_i^t} & \dot{x}_i^t \geq R_i \omega_i \\ \frac{R_i \dot{s}_{xt,i} \omega_i^2 + \omega_i \ddot{x}_i^t}{\dot{x}_i^t} & \dot{x}_i^t < R_i \omega_i \end{cases} \quad (16)$$

Afterward, with the assumption of ideal estimation on the sliding surface the longitudinal acceleration \ddot{x}_i^t from (13) is replaced in (16), to calculate the estimated torque of each wheel as in equation (17), and the desired torque input of each wheel to involve the parametric and unmodeled uncertainties [30] is calculated as in equation (18).

$$\hat{T}_i = R_i \hat{f}_{xt,i} + I_{yt,i} \begin{cases} \dot{s}_{xt,i} \dot{x}_i^t / R_i + \omega_i [\dot{x}_{d,i}^t - \lambda_{T,i}(\dot{x}_i^t - \dot{x}_{d,i}^t)] / \dot{x}_i^t & \dot{x}_i^t \geq R_i \omega_i \\ R_i \dot{s}_{xt,i} \omega_i^2 / \dot{x}_i^t + \omega_i [\dot{x}_{d,i}^t - \lambda_{T,i}(\dot{x}_i^t - \dot{x}_{d,i}^t)] / \dot{x}_i^t & \dot{x}_i^t < R_i \omega_i \end{cases} \quad (17)$$

$$T_i = \hat{T}_i - K_{T,i} \text{sgn}(S_{T,i}) \approx \hat{T}_i - K_{T,i} \frac{1 - \exp(-\Phi_{T,i} S_{T,i})}{1 + \exp(-\Phi_{T,i} S_{T,i})} \quad (18)$$

Where $\text{sgn}(\cdot)$ represents the discontinuous sign function which is replaced by a sigmoid function with a boundary layer of thickness $\Phi_{T,i}$ due to chattering issues, and $K_{T,i}$ denotes the control gain. To incorporate the effects of lag in the actuators, a first-order transfer function is utilized as below.

$$G_{L_{T,i}}(s) = \frac{T_i^a(s)}{T_i(s)} = \frac{1}{1 + L_{T,i}s} \quad (19)$$

Where $T_i^a(t)$ stands for the actual torque acting on each wheel and $L_{T,i}$ is the time constant of the lag function.

3.1.1. Proof of Stability

In the first instance, a positive definite function, known as the Lyapunov candidate, is introduced for each wheel.

$$\Gamma_{T,i} = \frac{1}{2} S_{T,i}^2 > 0 \quad (20)$$

Now, we take the time derivative of (20) and then replace $\dot{S}_{T,i}$ from (13) in the resulting equation, which gives

$$\dot{\Gamma}_{T,i} = S_{T,i} [\dot{x}_i^t - \dot{x}_{d,i}^t + \lambda_{T,i}(\dot{x}_i^t - \dot{x}_{d,i}^t)] \quad (21)$$

One can solve (16) for \ddot{x}_i^t and replace it in (21). On the other hand, substituting the torque T_i from (18) and the estimated torque \hat{T}_i from (17) into the resulting equation, and some mathematical manipulations, gives the following equation for $\dot{\Gamma}_{T,i}$.

$$\dot{\Gamma}_{T,i} = S_{T,i} \frac{\dot{x}_i^t}{I_{yt,i} \omega_i} [R_i (\hat{f}_{xt,i} - f_{xt,i}) \dots \dots - K_{T,i} \text{sgn}(S_{T,i})] \quad (22)$$

Now, in order to justify the convergence of the

sliding surface $S_{T,i}$ to zero, the negative definite sliding condition is considered as $\dot{\Gamma}_{T,i} \leq -\eta_{T,i} |S_{T,i}|$, where $\eta_{T,i}$ is a positive constant parameter to adjust the maximum time to reach the sliding surface. In this way, it is guaranteed that the candidate function $\Gamma_{T,i}$ in (20) is a Lyapunov function and the stability of the torque controller is proved. In conclusion, by considering the upper limit of the uncertainty of longitudinal force as $|\hat{f}_{xt,i} - f_{xt,i}| < F_i$, and supremum of $I_{yt,i} \omega_i / \dot{x}_i^t$ as G_i , the range of control gain $K_{T,i}$ in (18) is obtained as bellow (the bounds of variation for quantities $I_{yt,i}$, \dot{x}_i^t , and ω_i in G_i are known).

$$K_{T,i} \geq G_i \eta_{T,i} + R_i F_i \quad (23)$$

3.2. Lateral Control: Front Steering Angles

The lateral motion of the AEV is taken into control by using the front steering angle δ_f . The steering angle is designed in such a way that the lateral error \tilde{y} which is a combination of the lateral position error and the heading error, converges to zero.

As depicted in Figure 2, the lateral velocity error $\dot{\tilde{y}}$ is defined by the projection of velocities of the vehicle's CG on the path's coordinates, as bellow.

$$\dot{\tilde{y}} = \dot{x} \sin \tilde{\psi} + \dot{y} \cos \tilde{\psi} - 0 \quad (24)$$

The reason for putting zero on the right-hand side of (24) is to emphasize that the desired lateral velocity is assumed zero, according to the assumption of the point mass model for the design of the reference path.

The heading error is defined as $\tilde{\psi} = \psi - \psi_d$. Then, the sliding surface which is defined as a linear combination of the lateral error and its derivative is characterized as follows.

$$S_\delta = \dot{\tilde{y}} + \lambda_\delta \tilde{y} = \dot{x} \sin \tilde{\psi} + \dot{y} \cos \tilde{\psi} + \lambda_\delta \tilde{y} \quad (25)$$

Where λ_δ is a positive constant parameter. Next, assuming an ideal estimation on the sliding surface, the time derivative of the sliding surface (25) is set to be zero, resulting in

$$\begin{aligned} \dot{S}_\delta = 0 \Rightarrow \dot{y} = -[\dot{x}\dot{\tilde{\psi}} + \lambda_\delta \dot{y}] \dots \\ \dots + (\ddot{x} - \dot{y}\dot{\tilde{\psi}} + \lambda_\delta \dot{x}) \tan \tilde{\psi} \end{aligned} \quad (26)$$

On the other hand, after the multiplication of

$$\hat{f}_{yt,f} = -\hat{f}_{xt,f} \tan \delta_{k-1} + mb \frac{\dot{x}\dot{\psi}_a + \frac{I_{zz}}{mb} \ddot{\psi} - \lambda_\delta \dot{y} - (\ddot{x} - \dot{y}\dot{\tilde{\psi}} + \lambda_\delta \dot{x}) \tan \tilde{\psi}}{L \cos \delta_{k-1}} \quad (28)$$

The symbol (^) in (28) refers to the estimated value of the corresponding variable. Given that the steering angle is not specified yet, the estimated steering angle one step behind δ_{k-1} is replaced in (28). Recall that the lateral force in (7) is a non-linear function of lateral slip, as $\alpha_i = g^{-1}(f_{yt,f})$. Therefore, solving the inverse dynamics of the front tire of the nonlinear bicycle model gives the estimated value of the steering angle.

$$\hat{\delta}_f = g^{-1}(\hat{f}_{yt,f}) + \tan^{-1}(\dot{y} + a\dot{\psi}/\dot{x}) \quad (29)$$

It should be emphasized that with the assumption of a small steering angle, the lateral force of the front wheel lies in the linear region so that a linear relation exists between $f_{yt,f}$ and α_f . This assumption will be utilized for the proof of stability, later. Now, to incorporate the possible uncertainties, the equivalent control input of the steering angle is achieved [30].

$$\delta_f \approx \hat{\delta}_f - K_\delta \frac{1 - e^{-\Phi_\delta S_\delta}}{1 + e^{-\Phi_\delta S_\delta}} \quad (30)$$

Where K_δ stands for the control gain, and the sign function is approximated by a sigmoid function with a boundary layer of thickness Φ_δ to attenuate the chattering that arose due to the switching law. The steering angle acquired in (30) is the ideal control input. In order to impose the effects of the lag in actuators, the lag transfer

(7-a) by b , then adding both sides of the resulting equation to (7-b), results in

$$\begin{aligned} \ddot{y} = -\dot{x}\dot{\psi} - \frac{I_{zz}}{mb} \ddot{\psi} + \frac{L}{mb} [f_{yt,f} \cos \delta_f \dots \\ \dots + f_{xt,f} \sin \delta_f] \end{aligned} \quad (27)$$

Where $L = a + b$ points out the longitudinal distance between the front and rear axles. Now, equating both sides of (26) and (27) leads to the following relation for the sum of the front wheel's lateral forces.

function $G_{L_\delta}(s)$ is introduced.

$$G_{L_\delta}(s) = \frac{\delta_f^a(s)}{\delta_f(s)} = \frac{1}{1 + L_\delta s} \quad (31)$$

Where L_δ denotes the time constant of the lag function and $\delta_f^a(s)$ is the actual steering angle.

3.2.1. Proof of Stability

We consider a positive definite function Γ_δ as bellow.

$$\Gamma_\delta = \frac{1}{2} S_\delta^2 > 0 \quad (32)$$

Taking the time derivative of (32), then replacing \dot{S}_δ from (26) into the resulting equation, gives

$$\begin{aligned} \dot{\Gamma}_\delta = S_\delta [\dot{y}\dot{\tilde{\psi}} + (\ddot{x} - \dot{y}\dot{\tilde{\psi}} + \lambda_\delta \dot{x}) \sin \tilde{\psi} \dots \\ \dots + (\dot{x}\dot{\tilde{\psi}} + \lambda_\delta \dot{y}) \cos \tilde{\psi}] \end{aligned} \quad (33)$$

The acceleration \ddot{y} from (27) and the front lateral force $f_{yt,i}$ from (28), both are substituted into (33). On the other hand, replacing the steering angle δ_f from (30) and the estimated lateral force $\hat{f}_{yt,i}$ from (28) in the resulting equation, and some mathematical manipulations provide the following equation for $\dot{\Gamma}_\delta$.

$$\begin{aligned} \dot{\Gamma}_\delta = S_\delta \frac{L}{mb} \cos \tilde{\psi} \sin \delta_{k-1} [(\hat{f}_{xt,f} - f_{xt,f}) \\ \dots - K_\delta C_{\alpha,f} \cot \delta_{k-1} \operatorname{sgn}(S_\delta)] \end{aligned} \quad (34)$$

Now, considering the sliding condition as $\dot{\Gamma}_\delta \leq -\eta_\delta |S_\delta|$ the convergence of the sliding surface S_δ to zero is guaranteed, where η_δ represents a positive constant parameter. In addition, the negative definiteness of $\dot{\Gamma}_\delta$ is reserved, and the candidate function Γ_δ in (32) is a Lyapunov function which consolidates the stability of the steering controller.

Suppose that the upper limit of the uncertainty of front longitudinal force is $|\hat{f}_{xt,f} - f_{xt,f}| \leq F_f$, and the lower bound of cornering stiffness is C_{min} . The range of control gain K_δ in (30) is obtained as below.

$$K_\delta \geq C_{min}^{-1} (F_f + \frac{mb}{L} \eta_\delta) \quad (35)$$

4. Simulation Results and Analysis

4.1. Simulation Setup

The performance of the proposed control system is appraised by using a co-simulation in MATLAB\Simulink and Carsim software.

The AEV in Carsim not only incorporates the longitudinal and lateral motion of the vehicle, but also takes the DLT, experimental tire model, ride, pitch, roll, and other dynamics of the AEV into account. The vehicle in the Carsim software accommodates the whole actuators related to a D-Class SUV, including the four-wheel independent drive, independent brake, and front steering angles.

The parameters and dimensions of the AEV used in simulations are presented in Table 1, and Table 2 provides a list of the parameters have been utilized in the SMC controllers.

Table 1: List of the vehicle parameters.

Symbol	Quantity Description	Values
m	Vehicle mass	2009 kg
m_s	Sprung mass	1809 kg
I_{zz}	Vehicle mass moment of inertia	2000 kg.m ²
$I_{yt,i}$	Mass moment of inertia of each wheel	0.9 kg.m ²
a	Distance from CG to the front axle	1.56 m
b	Distance from CG to the rear axle	1.18 m
w	Track width	1.63 m
h_{CG}	The vertical distance from CG to ground	0.47 m
R_i	The effective radius of each tire	0.35 m
g	Gravitational acceleration	9.81 m/s ²
$C_{x,i}$	Longitudinal stiffness of each tire	95.3 kN
$C_{\alpha,i}$	Cornering stiffness of each tire	55.05 kN/rad

Table 2: Controller parameters in Simulations.

Symbol	Quantity Description	Values
$\lambda_{T,i}, \lambda_\delta$	Sliding surface parameters of SMCs	0.5 Hz , 0.5 Hz
$\eta_{T,i}, \eta_\delta$	Reaching time parameters of SMCs	5 m/s ² , 2 m/s ²
$\Phi_{T,i}, \Phi_\delta$	Boundary layer thicknesses of SMCs	1 s/m , 1 s/m
$L_{T,i}, L_\delta$	Time constants of the lag functions	0.15 s , 0.15 s

4.2. Validation and Comparison of the Results

The 7-DOF model of the vehicle in MATLAB is validated with its counterpart in the Carsim software. The model performance is evaluated in a sinusoidal maneuver, considering yaw rate and lateral acceleration. The results of yaw rate angles and lateral accelerations, considering the sine with dwell test [31], are presented in Figure 6. The initial velocity of the vehicle is set to be 70 km/h and the front steering angle includes three-quarters of a sine wave with the frequency of 0.7 Hz and magnitude of $5\pi/180$ rad, with a 0.5 s dwell.

The responses of lateral accelerations and yaw rates in Figure 6 have identical patterns which indicate good agreement between the 7-DOF model and the Carsim. While applying the sine with dwell steering input, the main reason for differences is that the vehicle's ride dynamics and pitch and roll effects are not included in the equations of the 7-DOF model and only the handling and wheel rotation dynamics are considered.

To evaluate the tracking performance of the proposed control system, the root mean square of errors and the maximum absolute value of the

errors (MAEs) are compared with one of the optimization-based studies. The RMSE for the error signal e is defined as $(\sum_i e_i^2/N)^{1/2}$, where N stands for the number of measurements. Two closed-loop control systems including the same reference path and the same Carsim AEV model, are simulated at the same time and the only different part is the controller block.

Table 3 represents the functionality of the proposed control system compared with the one in [32] which benefits from an optimization-based strategy. It can be observed that both controllers have shown good performance in following the reference path of lane-change. The RMSEs of the velocity error, longitudinal and lateral position errors have been better in our work. Although, the tracking performance of heading angle and yaw rate of [32] show better results.

4.3. Simulation Results and Discussion

Figure 7 demonstrates the capability of the proposed control system in the task of trajectory tracking. As in Figure 7, by using the proposed

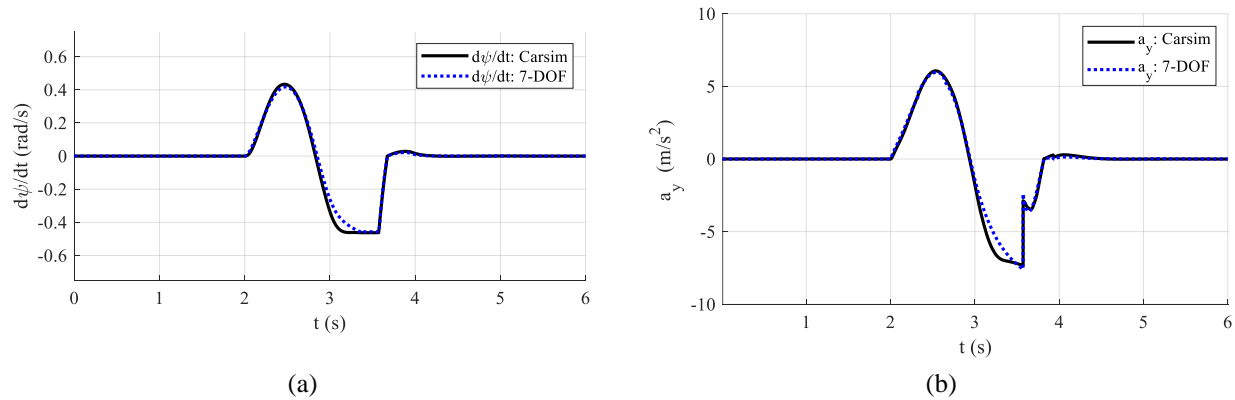


Figure 6: Validation of the 7-DOF model in MATLAB/Simulink with Carsim. (a) Yaw rate (b) Lateral acceleration.

Table 3: Comparison of the results, including RMSEs and MAEs).

Controller	e_x (m)		e_y (m)		e_v (m/s)		e_ψ (°)		$e_{\dot{\psi}}$ (°/s)	
	MAE	RMSE	MAE	RMSE	MAE	RMSE	MAE	RMSE	MAE	RMSE
Present Work	0.0265	0.0170	0.0470	0.0273	0.1547	0.1480	0.0596	0.0390	0.5575	0.2806
Reference [32]	0.0403	0.0232	0.2480	0.0617	0.3875	0.4356	0.224	0.0353	2.678	0.1519

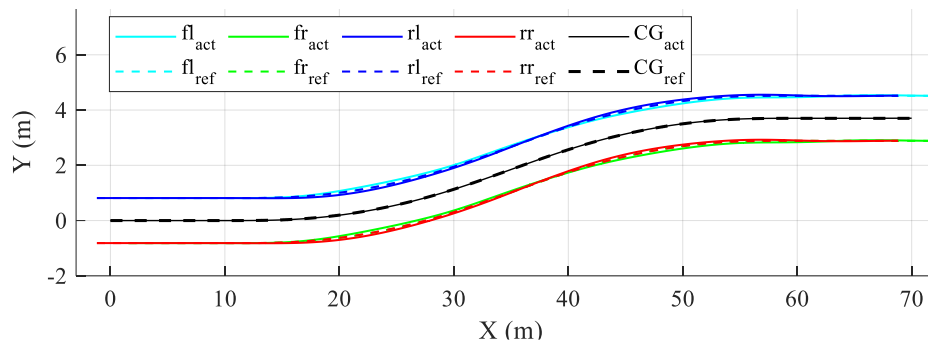


Figure 7: The reference path (ref) and the actual path (act) of each wheel, during the lane-change maneuver.

integrated controller each of the wheels follows the desired longitudinal and lateral position and the desired heading angle calculated by the kinematic constraints, while preserving the stability of the motion. At the beginning of the motion, the longitudinal and lateral position of the CG of the AEV is at the origin and over time, the two right wheels and the two left wheels track almost the same corresponding path obtained from kinematic relations.

All of the longitudinal and lateral errors are shown in Figure 8. As can be observed in Figure 8, the proposed controller enables the AEV to track the desired values of longitudinal and lateral position, velocity, heading angle, and yaw rate. In the transitional regions between the straight line, the clothoid, and the circular arc, the tracking errors demonstrate divergent behavior and tend to increase. However, the proposed controller identifies the parametric and modeling uncertainties causing the error divergence and makes them converge, which can be observed more clearly in Figure 8-b and Figure 8-d. As can be seen in Figure 8, the errors of the longitudinal and lateral positions and the velocity are limited to $[-2.6, 4]$ cm, $[-4.5, 3.3]$ cm, and $[-0.2, 0.4]$ m/s, respectively. The error signals for the heading angle and yaw rate lie in the bounds of $\pm 0.3^\circ$ and $\pm 2.7^\circ/\text{s}$, respectively. The results show that despite uncertainties of unmodeled dynamics occurring due to modeling of AEV in Carsim software and the lack of guarantee of accurate actuator commands, the proposed controller is capable of converging errors toward zero.

The side slip angle of the AEV and lateral slip of each wheel along with the lateral force acting on each wheel in terms of path parameter s are

shown in Figure 9. The right and left wheels of the front and rear axles have almost the same values of side slip and lateral force which validate the lateral dynamic model. Also, the small values of the slip angles illustrate that the tires are preserved in the linear region, which results in a good stability performance and reasonable torque distribution. As in Figure 9-b, in the first elementary path (10 to 35 m of the path), the rear slip angles take negative values and according to the nonlinear Pacejka combined slip tire model [27], the amount of theoretical lateral slip will become a positive value, therefore the control system provides large positive lateral forces for the rear wheels to compensate for the mentioned lateral slips. In the arc segments (17 to 29 m and 42 to 54 m of the path), the motion takes place on a constant curvature which demands a constant speed and as a result, generates constant lateral acceleration which needs pure cornering that requires an increasing lateral force. Then, the highest amount of lateral forces of the wheels in Figure 9-a, occurs on the mentioned arc segments of the path, as expected.

The control inputs to the AEV including the front steering angle and the driving or braking torques of each wheel are presented in Figure 10 and Figure 11, respectively. The lateral position error and the heading angle error of the AEV in the first and second elementary paths (10 to 35 m, and 35 to 60 m of the path) have negative and positive values, demanding positive and negative front steering angles to compensate these lateral errors, as in Figure 10.

Due to the initial zero value of the torque of each wheel, these torques tend to a steady value after passing a transient range in the straight

segment (0 to 10 m of the path), as shown in Figure 11. The straight segments (0 to 10 m and 60 to 70 m of the path) demand pure braking and pure acceleration without any need to steering, which is justified in Fig. 10 and Figure 11. The arc segments (17 to 29 m and 42 to 54 m) demand only the steering angle. The combined driving /braking torque and front steering angle are anticipated for the clothoid segments (10 to 17 m, 29 to 42 m, and 54 to 60 m of the path), which is justified in Fig. 10 and Figure 11.

Any circumstance that affects the vehicle's DLT and changes the position of the CG, may cause instability of the vehicle's motion in path tracking. The addition of one or more passengers to the AEV causes uncertainty in the inertial parameters, like mass and moments of inertia of the vehicle.

First, the case is investigated in which the AEV undergoes an uncertainty in the mass. A situation where four passengers on the front and

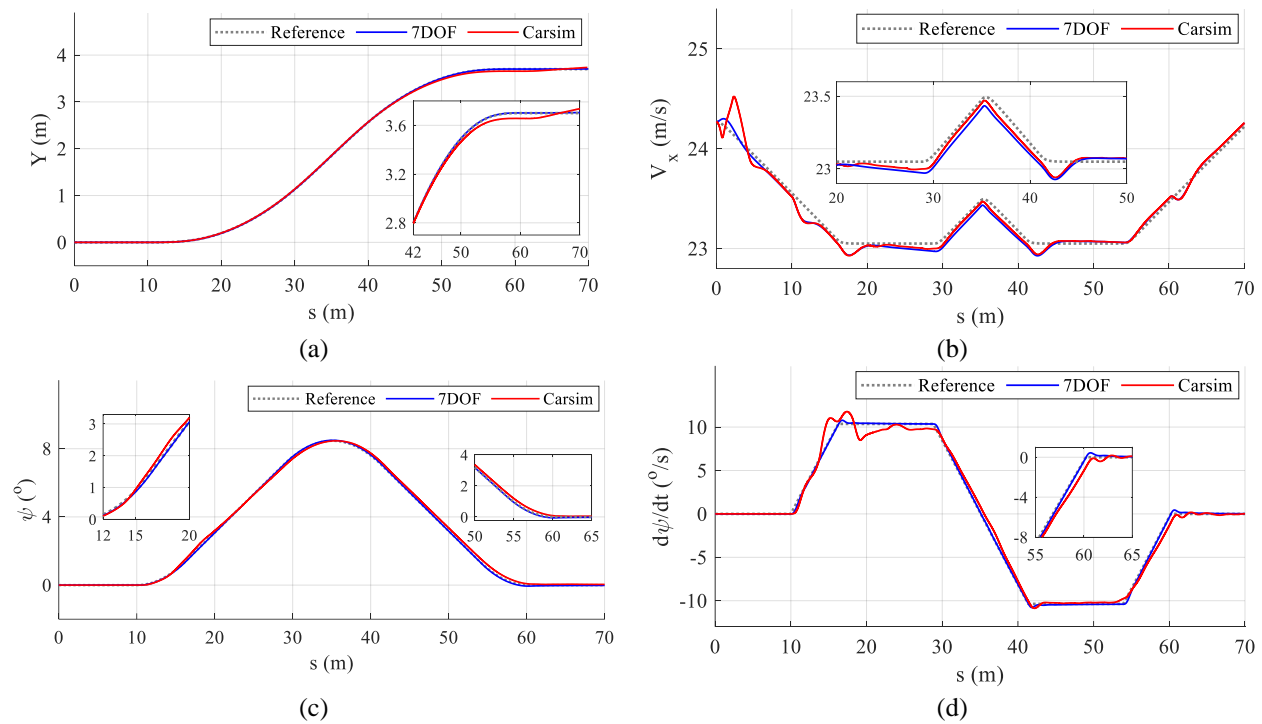
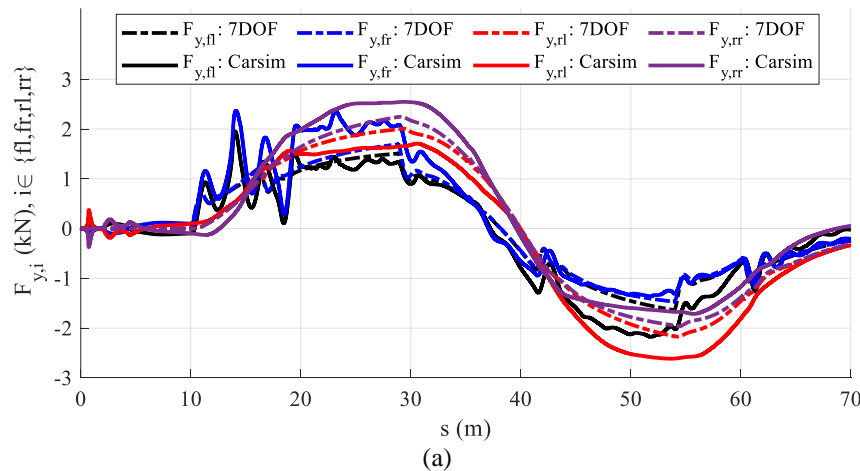


Figure 8: Tracking performance of the AEV. (a) Lateral position, (b) Velocity, (c) Heading angle, (d) Yaw rate.



(a)

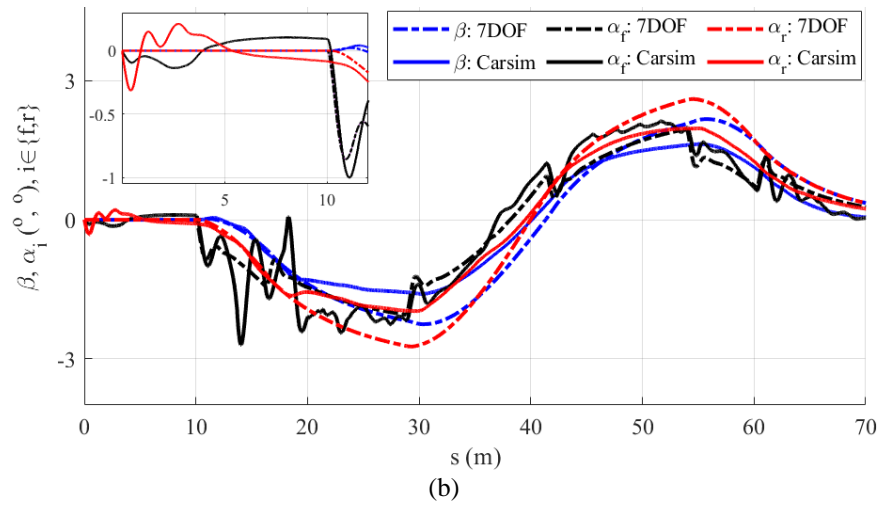


Figure 9: The lateral forces and slips. (a) Side slip angle β and slip angles α_i of the front and rear wheels, (b) Lateral forces generated by each wheel.

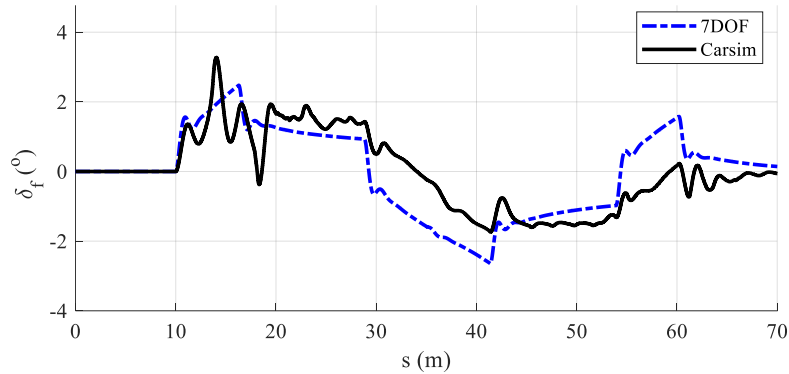


Figure 10: The front steering angle input δ_f .

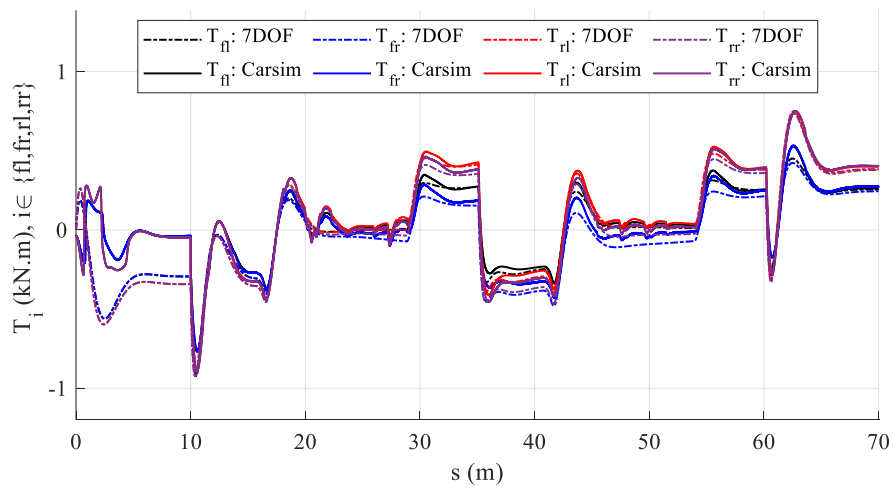


Figure 11: The driving / braking torque inputs T_i of each wheel.

back seats, and one payload in the trunk, each of weight 80 kg are added to the AEV in Carsim software. In the second case, a wind disturbance with amplitude of 50 km/h, and heading 90° to left and then 90° to right side of the AEV is imposed. And for the third case, we examined the change of friction coefficient between the road surface and the contact patch of each tire of the AEV, in the range of 0.6 to 0.85.

The performance of the proposed control system in the presence of the mentioned uncertainties is examined. It is necessary to emphasize that the maximum values of the parametric uncertainties in mass, wind, and

friction coefficient cannot be unbounded, and we run the simulation until we can find the largest possible extent of uncertainties that the control system is still able to perform the task of path following with acceptable errors.

Figure 12 indicates the robust performance of the proposed integrated control system which demonstrates the quality of trajectory tracking with maximum allowable tracking errors, in the presence of uncertainties. As can be observed in Figure 12, the proposed controller is able to handle the parametric uncertainties and also is able to keep the maximum amplitude of tracking errors within admissible ranges.

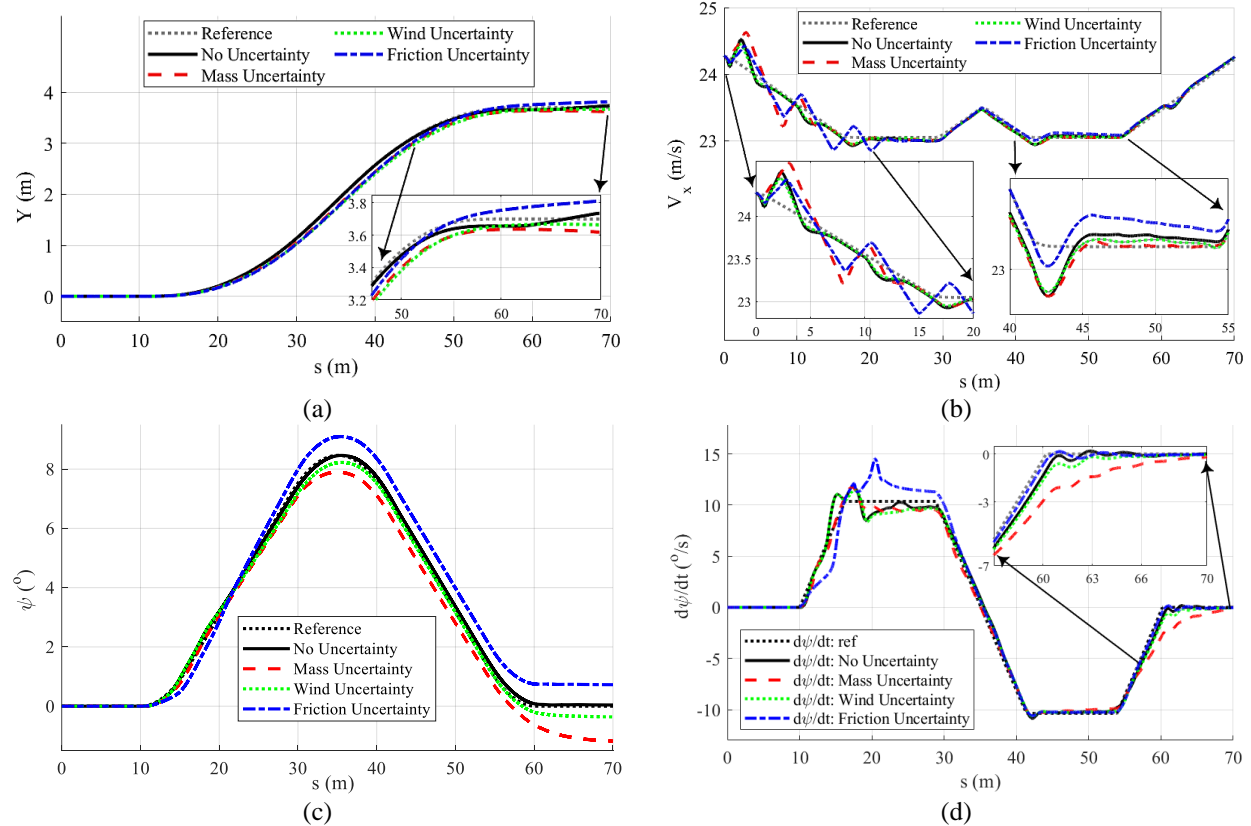


Figure 12: The results of tracking errors in the presence of wind, friction, and mass uncertainties. (a) Position errors, (b) Velocity errors, (c) Heading angle errors, (d) Yaw rate errors.

5. Conclusions

The main purpose of this paper is to design a control system that assigns the individual torque for each wheel of the AEV along with the front steering commands to follow a reference path. To fulfill this purpose, a Kinematic-based

approach is proposed for the actuator constraints of each wheel. The simulation results show the capability of the proposed controller in path following task, and ensure the stability of the control system. In addition, the proposed SMCs generate the driving or braking torque of each wheel in presence of parametric uncertainties.

The advantage of this method is to ignore iterative optimization techniques proposed in the literature. Furthermore, the calculations in the process of control design are based on the data that can be measured by sensors or estimated by the mathematical models. The future path of this study is to develop and analyze different control methodologies, including robust, optimal, fault tolerant, etc., in the task of trajectory tracking in various road conditions and various driving states.

Declaration of Conflicting Interests

The author(s) declared no potential conflicts of interest with respect to the research, authorship, and/or publication of this article.

References

- [1] S. Li, X. Zhu, Y. Ma, F. Zhang, H. Zhou, The Role of Government in the Market for Electric Vehicles: Evidence from China, *J. Policy Analysis and Management*, Vol.41, No.2, (2022), pp.450-485.
- [2] D. Rimpas, S. D. Kaminaris, I. Aldarraji, D. Piromalis, G. Vokas, P.G. Papageorgas, G. Tsaramirsis, Energy management and storage systems on electric vehicles: A comprehensive review, *Materials Today: Proceedings*, Vol.61, (2022), pp.813-819.
- [3] O. Sadeghian, A. Oshnoei, B. Mohammadi-ivatloo, V. Vahidinasab, A. Anvari-Moghaddam, A comprehensive review on electric vehicles smart charging: solutions, strategies, technologies, and challenges, *J. Energy Storage*, Vol.54, (2022), pp.1-24.
- [4] H. Salmani, M. Abbasi, T. Fahimi Zand, M. Fard, R. Nakhaie Jazar, A new criterion for comfort assessment of in-wheel motor electric vehicles, *J. Vibration & Control*, Vol.28, No.3-4, (2022), pp.316-328.
- [5] A. H. Ahangarnejad, A. Radmehr, M. Ahmadian, A review of vehicle active safety control methods: from antilock brakes to semiautonomy, *J. Vibration & Control*, Vol.27, No.15-16, (2020), pp.1683-1712.
- [6] Q. Wang, Y. Zhao, Y. Deng, H. Xu, H. Deng, F. Lin, Optimal coordinated control of ARS and DYC for four-wheel steer and in-wheel motor driven electric vehicle with unknown tire model, *IEEE Trans. Vehicular Technology*, Vol.69, No.10, (2020), pp.10809-10819.
- [7] A. Barari, S. Saraygord Afshari, X. Liang, Coordinated control for path-following of an autonomous four in-wheel motor drive electric vehicle, *Proc. Instit. Mech. Eng., Part C: J. Mechanical Engineering Science*, Vol.236, No.11, (2022), pp.6335-6346.
- [8] K. Nam, H. Fujimoto, Y. Hori, Lateral stability control of in-wheel-motor-driven electric vehicles based on sideslip angle estimation using lateral tire force sensors, *IEEE Trans. Vehicular Technology*, Vol.61, No.5, (2012), pp.1972-1985.
- [9] W. Han, A. Li, X. Huang, W. Li, J. Cao, H. Bu, Trajectory tracking of in-wheel motor electric vehicles based on preview time adaptive and torque difference control, *J. Advances in Mechanical Engineering*, Vol.14, No.4, (2022), pp.1-16.
- [10] H. Rahmani, A. Aliabadi, A. Ghaffari, S. Azadi, Multi-input sliding mode control for path following in four wheel steering autonomous vehicles, *30th Annual Int. Conf. Iranian Society Mech. Engineers*, Tehran, Iran, (2022).
- [11] H. Rahmani, A. Aliabadi, A. Ghaffari, S. Azadi, Lyapunov-based path following of four wheel steering autonomous vehicles, *30th Annual Int. Conf. Iranian Society Mech. Engineers*, Tehran, Iran, (2022).
- [12] A. Ghaffari, S. H. Tabatabaei Oreh, R. Kazemi, R. Karbalaie M.A., An intelligent approach to the lateral force usage in controlling the vehicle yaw rate, *Asian J. Control*, Vol.13, (2011), pp.213-231.
- [13] S. Azadi, R. Kazemi, H. R. Nedamani, *Vehicle dynamics and control: Advanced methodologies*, Elsevier Ltd., (2021).
- [14] A. N. Asiabar, R. Kazemi, A direct yaw moment controller for a four in-wheel motor drive electric vehicle using adaptive sliding mode control, *Inst. Mech. Eng., J. Multi-body Dynamics*, Vol.233, (2019), pp.549-567.

- [15] H. Park, Optimal tire force allocation for autonomous trajectory tracking, Ph.D Thesis, Stanford University, USA, (2017).
- [16] C. Xiang, H. Peng, W. Wang, L. Li, Q. An, S. Cheng, Path tracking coordinated control strategy for autonomous four in-wheel-motor independent-drive vehicles with consideration of lateral stability, *Proc. Instit. Mech. Eng., Part D: J. Automobile Engineering*, Vol.235, No.4, (2020), pp.1023-1036.
- [17] H. Park, J. C. Gerdes, Analysis of feasible tire force regions for optimal tire force allocation with limited actuation, *IEEE Intel. Trans. Syst. Magazine*, Vol.9, (2017), pp.75-87.
- [18] L. Zhai, C. Wang, Y. Hou, C. Liu, MPC-based integrated control of trajectory tracking and handling stability for intelligent driving vehicle driven by four hub motor, *IEEE Trans. Vehicular Technology*, Vol.71, No.3, (2022), pp.2668-2680.
- [19] X. Li, N. Xu, K. Guo, Y. Huang, An adaptive SMC controller for EVs with four IWMs handling and stability enhancement based on a stability index, *Vehicle System Dynamics*, Vol.59, No.10, (2021), pp.1509-1532.
- [20] L. Guo, P. Ge, D. Sun, Torque distribution algorithm for stability control of electric vehicle driven by four in-wheel motors under emergency conditions, *IEEE Access*, Vol.7, (2019), pp.104737-104748.
- [21] Y. Tong, C. Li, G. Wang, H. Jing, Integrated path-following and fault-tolerant control for four-wheel independent-driving electric vehicles, *Automot. Innov.*, Vol.5, (2022), pp.311-323.
- [22] B. Gao, Y. Yan, H. Chu, H. Chen, N. Xu, Torque allocation of four-wheel drive EVs considering tire slip energy, *Science China Information Sciences*, Vol.65, (2021), p.1222021-14.
- [23] W. Chen, H. Zhao, J. Zhao, Y. Feng, H. Chen, Integrated control of longitudinal-vertical force for distributed electric vehicles, *Chinese Cont. and Decision Conf. (CCDC)*, (2019), pp.218-223.
- [24] Y. Luo, K. Cao, K. Li, Coordinated control of longitudinal/lateral/vertical tire forces for distributed electric vehicles, *American Cont. Conf. (ACC)*, (2014), pp.3905-3910.
- [25] Y. Dai, Y. Luo, W. Chu, K. Li, Optimum tyre force distribution for four-wheel-independent drive electric vehicle with active front steering, *Int. J. Vehicle Design*, Vol.65, No.4, (2014), pp.336-359.
- [26] S. Tashakori, S. Kasiri Bidhendi, B. Mashadi, J. Marzbanrad, Trajectory control and sensitivity analysis of curiosity rover on uneven terrains, *J. Dynamic Systems, Measurement, and Control*, Vol.141, (2019), pp.111001 1-13.
- [27] H. Pacejka, I. J. M. Besselink, *Tire and Vehicle Dynamics*. Elsevier Science, (2012).
- [28] J. Funke, J. C. Gerdes, Simple clothoid lane change trajectories for automated vehicles incorporating friction constraints, *J. Dynamic Systems, Measurement and Control*, Vol.138, No.2, (2015), p.0210021-9.
- [29] I. Bae, J. Moon, J. Jhung, H. Suk, T. Kim, H. G. Park, J. Cha, J. W. Kim, D. S. Kim, S. Kim, Self-driving like a human driver instead of a robocar: personalized comfortable driving experience for autonomous vehicles, *33rd Conf. Neur. Info. Proces. Syst. (NeurIPS)*, Vancouver, Canada, (2019).
- [30] J. E. Slotine, W. Li, *Applied Nonlinear Control*, Prentice-Hall, (1991).
- [31] K. Chatrath, Vehicle dynamics control using control allocation, M.Sc. Thesis, TU Delft, Netherlands, (2019).
- [32] H. Park, J. C. Gerdes, Optimal tire force allocation for trajectory tracking with an over-actuated vehicle, *IEEE Intelligent Vehicles Symposium (IV)*, (2015), pp.1032-1037.